RSC Advances

PAPER

View Article Online
View Journal | View Issue

Cite this: *RSC Adv.*, 2025, **15**, 29692

Fungal laccase-guided copper nanoflower assembly enables complete conversion of HMF to FDCA

Lei Yang, †[a] Anbang Duan,†[a] Yuan Ding,[ac] Xiquan Song,[b] Qianli Ma,[b] Zhanyin Liu,[a] Tingying Wei,[a] Zhixing Wang*[a] and Chunzhao Liu *[a]

The growing demand for sustainable biomanufacturing has driven significant interest in 2,5-furandicarboxylic acid (FDCA), a bio-based platform chemical for producing renewable polymers. The eco-friendly oxidoreductase laccase exhibits promising FDCA biosynthesis capacity yet is hampered by pH-dependent activity decay and susceptibility to proteolytic degradation. Herein, we developed a bio-enabled synthesis approach to fabricate three-dimensional laccase-integrated copper hybrid nanoflowers (Lac-NFs) through enzyme–metal coordination-driven self-assembly. The engineered Lac-NFs displayed high enzyme encapsulation efficiency (89.28%) and enhanced environmental robustness compared to free laccase. Furthermore, the Lac-NFs maintained prolonged storage stability with well-preserved activity relative to the native enzyme. Elevated catalytic efficiency and refined enzymatic kinetics were achieved *via* copper-mediated electron transfer networks within the hybrid matrix. Remarkably, Lac-NFs demonstrate exceptional catalytic efficiency and selectivity in the conversion of HMF to FDCA, achieving complete substrate conversion under precisely controlled operational parameters. This nano–biohybrid design establishes a robust and efficient biocatalytic platform for biomass valorization into high-value-added chemicals, exhibiting promising scalability prospects for industrial implementation.

Received 13th June 2025
Accepted 12th August 2025

DOI: 10.1039/d5ra04187b

rsc.li/rsc-advances

1. Introduction

While fossil fuel utilization has served as the foundational pillar of modern industrialization, its dual-edged nature becomes increasingly apparent. Paradoxically, this energy regime has driven unprecedented technological innovation and socioeconomic development, whereas it has simultaneously triggered accelerating environmental deterioration and irreversible resource depletion.[1] This inherent contradiction highlights the critical imperative for transitioning to sustainable alternatives, with biomass-derived platform chemicals emerging as strategically vital candidates in this paradigm shift.[2] The U.S. Department of Energy designated 12 biomass-derived compounds as strategic platform chemicals for synthesizing high-value-added products as early as 2004.[3] Among them, 2,5-furandicarboxylic acid (FDCA) stands out as a structural mimic of petroleum-based terephthalic acid (TPA) with superior sustainability credentials. Comparative analysis reveals that FDCA-derived polyethylene furanoate (PEF) outperforms conventional polyethylene terephthalate (PET) in both biodegradation kinetics and production-phase emission reduction.[4,5] These compelling metrics establish FDCA as the prime candidate for green polymer synthesis and a linchpin in circular economy strategies.[6]

The roadmap to FDCA production predominantly traverses through hydroxymethylfurfural (HMF), a carbohydrate-derived "chassis molecule" bearing three reactive sites: furan ring, hydroxymethyl, and formyl groups.[7] Strategic oxidation of these moieties enables two distinct pathways to FDCA: pathway I involves the oxidation of HMF to 2,5-diformylfuran (DFF), which is subsequently further oxidized to 2-formyl-5-furancarboxylic acid (FFCA), ultimately yielding 2,5-furandicarboxylic acid (FDCA).[8] In contrast, Pathway II sequentially oxidizes HMF's aldehyde group to carboxyl (forming HMFCA), then hydroxyl to aldehyde (yielding FFCA), ultimately producing FDCA.[9] Breakthroughs in interfacial engineering have propelled FDCA synthesis beyond traditional efficiency limits, with precision-controlled oxidation cascades now achievable through tailored catalytic architectures. Klinyod *et al.* developed an alkaline-stable electrocatalyst using NiNPs/GO-Ni-foam, achieving 86.9% ± 4.1% FDCA yield through electrochemical treatment. Parallel innovations by Li *et al.* fabricated Au/TiO_2

[a]*State Key Laboratory of Bio-fibers and Eco-Textiles, Institute of Biochemical Engineering, The 3rd Clinical College of Qingdao University, College of Materials Science and Engineering, Qingdao University, Qingdao 266071, China. E-mail: wangzhixing@qdu.edu.cn; czliu@qdu.edu.cn*

[b]*Tayho Advanced Materials Group Co. Ltd., Yantai, 264006, China*

[c]*Department of Sports Medicine, Qingdao Municipal Hospital, Qingdao 266071, China*

† Lei Yang and Anbang Duan contributed equally.

nanocomposites *via* the urea deposition method and subsequently functionalized them with iron phthalocyanine (FePc) through ball milling to synthesize FePc/Au–TiO_2 heterostructures.[10,11] The optimized catalyst with 30 wt% FePc after calcination at 410 °C demonstrated exceptional photocatalytic performance, achieving a remarkable FDCA yield of 97%. While significant progress has been achieved, existing approaches remain constrained by energy-demanding operational parameters (elevated temperature/pressure) and dependence on noble metal catalysts, emphasizing the demand for energy-efficient catalytic platforms operating under mild conditions. In this catalytic context, enzymatic strategies demonstrate unique advantages through room-temperature processing capabilities, intrinsic molecular recognition selectivity, and sustainable process attributes.[12]

Recent breakthroughs in enzymatic HMF-to-FDCA conversion highlight the potential of orchestrated multi-enzyme cascades systems. Swoboda *et al.* developed a compartmentalized cascade using *Marasmius oreades* and *Pleurotus ostreatus* unspecific peroxygenases (UPOs), achieving 99% FDCA yield *via* spatially resolved HMF → FFCA → FDCA oxidation.[13] However, enzyme loading ratios and mass transfer limitations in such one-pot systems necessitate energy-intensive parameter optimization, further increasing production expenses for industrial-scale applications. Single-enzyme systems, while operationally simpler, also exhibit intrinsic performance limitations. Mono-enzymatic approaches often fail to achieve complete substrate oxidation, arrested at intermediates stages due to inherently constrained catalytic promiscuity arising from narrow substrate specificity and inadequate activation energy landscapes for successive oxidative transformations.[14]

The blue multicopper oxidases laccases (EC 1.10.3.2), primarily found in fungi and plants, offer several advantages over conventional catalysts, including high selectivity and broad substrate adaptability, with water as their sole by-product.[15] The oxidative capacity of laccases is intrinsically governed by their redox potential, with *Trametes versicolor* laccase (TvL) demonstrating exceptional catalytic prowess through its elevated 780 mV redox potential (*vs.* NHE) – a functional superiority over most bacterial/plant orthologs.[16] This catalytic efficacy is synergistically augmented through redox mediators such as 2,2,6,6-tetramethylpiperidine-1-oxyl (TEMPO), which not only amplify the enzyme's oxidative potential to broaden substrate inclusivity toward HMF but also establish a self-regenerating catalytic cycle.[17] The above properties position TvL as the biocatalyst of choice for HMF valorization. However, practical implementation of free laccases still faces many critical limitations, such as poor operational stability, narrow pH/temperature tolerance, and difficult recovery.[18] To address these issues, immobilization strategies have gained prominence. For example, Wang *et al.* reported a magnetically immobilized laccase system with 90.2% FDCA yield after 96 h, while Chang *et al.* achieved a breakthrough 98.6% FDCA yield within 10 h using MOF-immobilized CotA laccase.[19,20]

Among emerging immobilization approaches, enzyme–inorganic hybrid nanoflowers are distinguished by their hierarchical porous architecture and augmented mass transfer capabilities.[21] In copper-based systems, enzyme-templated self-assembly forms flower-like nanostructures through heterogeneous nucleation of copper phosphate crystals at Cu^{2+} sites on laccase surfaces. Beyond providing nucleation centers, laccase molecules direct anisotropic crystal growth *via* spatial confinement and templating effects of their surface structures. This yields fully developed branched nanoarchitectures through kinetically controlled anisotropic growth.[21,22] In the present study, we reported bioinspired immobilization strategy exploiting enzyme–inorganic nanohybrids. Laccase-$Cu_3(PO_4)_2 \cdot 3H_2O$ nanoflowers (Lac-NFs) are architected through coordination-driven self-assembly of laccase molecules and morphology-controlled mineralization with Cu^{2+}/PO_4^{3-}. Systematic optimization of laccase/Cu^{2+} ratios yielded hierarchically structured nanoflowers with enhanced catalytic performance. The activities of free laccase and Lac-NFs under different temperature and pH conditions, as well as their storage stability at various temperatures, were further examined. Most critically, the complete transformation of HMF to FDCA was accomplished after 42 h through systematic process optimization. This streamlined process minimizes downstream purification burdens owing to the significantly reduced formation of intermediate by-products, thereby demonstrating substantial potential for industrial-scale applications.

2. Materials and methods

2.1 Chemicals and reagents

Laccase was produced from laboratory-cultured *T. versicolor*. Agar powder and potato dextrose broth were purchased from Qingdao Haibo Biotechnology Co., Ltd. Copper sulfate pentahydrate ($CuSO_4 \cdot 5H_2O$), disodium hydrogen phosphate dodecahydrate ($Na_2HPO_4 \cdot 12H_2O$), sodium dihydrogen phosphate dihydrate ($NaH_2PO_4 \cdot 2H_2O$), magnesium sulfate heptahydrate ($MgSO_4 \cdot 7H_2O$), ammonium dihydrogen phosphate ($NH_4H_2PO_4$), ferrous sulfate heptahydrate ($FeSO_4 \cdot 7H_2O$), ammonium chloride (NH_4Cl), glucose, concentrated phosphoric acid (H_3PO_4), sodium chloride (NaCl), potassium dihydrogen phosphate (KH_2PO_4), calcium chloride dihydrate ($CaCl_2 \cdot 2H_2O$), and ethanol (95%) were purchased from Sinopharm Chemical Reagent Co., Ltd. 2,2,6,6-Tetramethylpiperidin-1-oxyl (TEMPO), 2,2′-azino-bis(3-ethylbenzothiazoline-6-sulfonic acid) diammonium salt (ABTS), and Coomassie Brilliant Blue G-250 (BBG) were purchased from Macklin Biochemical Co., Ltd. 5-Hydroxymethylfurfural (HMF), 2,5-diformylfuran (DFF), 5-formyl-2-furancarboxylic acid (FFCA), and 2,5-furandicarboxylic acid (FDCA) were purchased from Aladdin Industrial Corporation. All chemicals were of analytical grade and used without further purification.

2.2 Laccase acquisition

T. versicolor was initially cultured on a slant medium at 26 °C for 7 days to promote mycelium formation. Subsequently, an appropriate amount of mycelium was transferred to a liquid medium and incubated at 26 °C with shaking at 150 rpm for 7

days to generate primary seeds. The primary seeds were homogenized and further incubated for 5 days to produce secondary seeds. These secondary seeds were then homogenized and inoculated into the fermentation broth, followed by incubation at 26 °C with shaking at 150 rpm for 7 days. Prior to fermentation, the pH of the medium was adjusted to 4.0; during fermentation, the pH was maintained at 4.0 by adding 0.1 M HCl or 0.1 M KOH as needed. The supernatant obtained after filtration was collected as the laccase solution. To enhance laccase activity, the inducer farnesol was added on the first day of fermentation.

2.3 Preparation of nanoflowers

The nanoflowers were prepared following a previously reported method.[21] Briefly, 1.45 g of disodium hydrogen phosphate dodecahydrate ($Na_2HPO_4 \cdot 12H_2O$), 0.15 g of sodium dihydrogen phosphate dihydrate ($NaH_2PO_4 \cdot 2H_2O$), and 0.5 g of sodium chloride (NaCl) were dissolved in 500 mL of deionized water to prepare a 10 mM phosphate buffer solution (PBS, pH 7.4), which was then set aside. Subsequently, a 5–17.5 mM copper sulfate pentahydrate solution, 25–125 μg mL^{-1} free laccase, and PBS were sequentially added to the reaction system. The mixture was stirred at 120 rpm for 5 minutes and incubated at 4 °C for 48 hours to form blue precipitates (Lac-NFs). The precipitates were washed three times with deionized water and centrifuged at 4000 rpm and 4 °C. To investigate the influence of nanoflower structure on the experimental results, bovine serum albumin nanoflowers (Bsa-NFs) were prepared using the same procedure as for the laccase nanoflowers.

2.4 Characterization of nanoflowers

The morphological features of Lac-NFs were observed using a cold field emission scanning electron microscope (SEM, S-4800, Hitachi, Japan). The crystal structure was determined using a multifunctional powder X-ray diffractometer (Malvern Panalytical), and the diffraction patterns were obtained in continuous scanning mode within the range of 5–85° at a scanning rate of 0.1° per second. Additionally, the surface elemental binding energies of the synthesized Lac-NFs were analyzed by X-ray photoelectron spectroscopy (XPS) to determine the physicochemical properties, such as chemical composition and chemical valence states, of the material surface. Furthermore, the carrier functional groups were analyzed using an FTIR-8400S Fourier transform infrared spectrometer to confirm the successful immobilization of laccase.

2.5 Determination of laccase activity

ABTS was used as a substrate to determine laccase activity.[23] A total volume of 1 mL was prepared by mixing 0.1 mM ABTS with 0.1 M sodium tartrate buffer (pH 4.0) and adding an appropriate amount of free or immobilized laccase. The mixture was shaken at 26 °C for 3 minutes, followed by separation of the suspension. The absorbance of the supernatant was measured at 420 nm using a UV-2000 spectrophotometer. Enzyme activity was defined as the amount of laccase required to oxidize 1 μM ABTS per minute, which corresponds to one unit of enzyme activity (U). The formula was calculated as follows, and all measurements were repeated three times and averaged.

$$U\ (\mathrm{U\ L^{-1}}) = \frac{\Delta \mathrm{OD}_{420} \times 10^6 \times V_s \times n}{\varepsilon \times \Delta T \times V_t \times d} \quad (1)$$

where ΔOD_{420} is the difference in absorbance between the sample and the blank control at 420 nm; ε is the molar extinction coefficient of ABTS (36 000 L mol^{-1} cm^{-1}); V_t and V_s (L) represent the total volume of the reaction system and the volume of laccase, respectively; ΔT (min) is the reaction time; d is the optical path length (1 cm); and n is the number of dilutions.

2.6 Determination of laccase encapsulation yield

The laccase encapsulation yield (EY) was determined following a previously reported method.[24] First, a bovine serum albumin (BSA) solution with a concentration of 0.1 mg mL^{-1} was prepared and diluted to a range of 10–100 μg mL^{-1} to generate a series of standard protein solutions. Then, 50 μL of the standard protein solution was mixed with 250 μL of Coomassie Brilliant Blue G250 staining solution and thoroughly shaken to ensure homogeneous mixing. The reaction solution was incubated at 25 °C for 5 minutes, and the absorbance was measured at 595 nm. As a control, 50 μL of deionized water was mixed with 250 μL of G250 staining solution, and the absorbance was measured under the same conditions. A standard curve of absorbance *versus* protein concentration was plotted using the obtained data (Fig. S-1). Subsequently, 50 μL of laccase solution was mixed with 250 μL of Coomassie Brilliant Blue G250 staining solution and incubated at 25 °C for 5 minutes. The absorbance was measured at 595 nm, and the corresponding protein concentration was calculated based on the standard curve. The encapsulation rate (EY) of laccase was calculated using the following formula:

$$\mathrm{EY} = \frac{A_1 - A_2 - A_3}{A_1} \quad (2)$$

where A_1 is the concentration of added laccase (mg mL^{-1}), A_2 is the concentration of laccase in the supernatant (mg mL^{-1}), and A_3 is the concentration in the wash supernatant (mg mL^{-1}).

2.7 Determination of laccase kinetic constant

Reaction solutions were prepared by dissolving ABTS in sodium tartrate buffer (pH 4.0) at concentrations of 0.015625 mM, 0.03125 mM, 0.0625 mM, 0.125 mM, 0.25 mM, and 0.5 mM. Subsequently, the kinetic constants (K_m) and maximum reaction rates (V_m) of the enzymatic reactions of free and immobilized laccase were determined, and linear regression analysis was performed using Lineweaver–Burk plots.[25] The formulae were calculated as follows:

$$\frac{1}{V} = \frac{K_m}{V_m} \times \frac{1}{S} + \frac{1}{V_m} \quad (3)$$

where V is the enzymatic reaction rate (mM); K_m is the Michaelis–Menten constant (mM); V_m maximum reaction rate

(mM min^{-1}) and S substrate concentration (mM). The kinetic parameters K_m and V_m were calculated from the slope and intercept, respectively.

2.8 Effect of temperature and pH on laccase activity

The effect of temperature (20, 30, 40, 50, and 60 °C) on laccase activity was investigated at pH 4.0. Additionally, the effect of different pH values (3.0, 4.0, 5.0, 6.0, 7.0, and 8.0) on laccase activity was further examined at the optimum temperature.

2.9 Storage stability

Under optimal conditions, free laccase and Lac-NFs were stored in PBS (10 mM, pH 6.0) at 4 °C and 25 °C, respectively. The residual activity of the samples was measured at regular intervals, and the storage stability was evaluated by defining the initial activity as 100%.

2.10 Catalytic oxidation of HMF

HMF and TEMPO were dissolved in 1 mL of nanoflower PBS buffer to achieve final concentrations of 10 mM and 30 mM, respectively. The reaction was performed by stirring the mixture at 120 rpm with aeration for 2 minutes at 1 hour intervals for 12 hours at 30 °C. The samples were analyzed using high-performance liquid chromatography (Agilent Infinity II LC) equipped with a UV detector and a C18 column (Diamonsil). The reacted samples were diluted 50-fold with PBS buffer, filtered through a 0.22 μm membrane, and then analyzed. The analytical conditions were as follows: the mobile phase consisted of an aqueous solution containing 0.1% trifluoroacetic acid and acetonitrile (85 : 15, v/v), the column temperature was 40 °C, the flow rate was 0.15 mL min^{-1}, and the injection volume was 20 μL. The detection wavelengths for HMF, DFF, FFCA, and FDCA are shown in Fig S-2, and the calibration curves of the standards (HMF, DFF, FFCA, and FDCA) are shown in Fig S-3. The retention times and detection wavelengths of each substance are presented in Fig S-4 and Table S-1. HMF was dissolved in 10 mM PBS buffer (pH 4.0, 6.0, and 8.0) to a concentration of 10 mM, with TEMPO as a mediator, and catalyzed by Lac-NFs. The reaction was carried out continuously for 36 hours at 30 °C and 120 rpm. A single-factor experimental design was employed to investigate the effects of pH, temperature, and TEMPO concentration on the catalytic efficiency of Lac-NFs toward HMF. The TEMPO concentration ranged from 5 to 40 mM, and the reaction temperature ranged from 20 to 60 °C, with continuous stirring at 120 rpm for 36 hours.

3. Results and discussion

3.1 Synthesis and characterization of Lac-NFs

3.1.1 Optimized fermentation of *T. versicolor* laccase and synthesis of Lac-NFs. Our previous studies demonstrated that

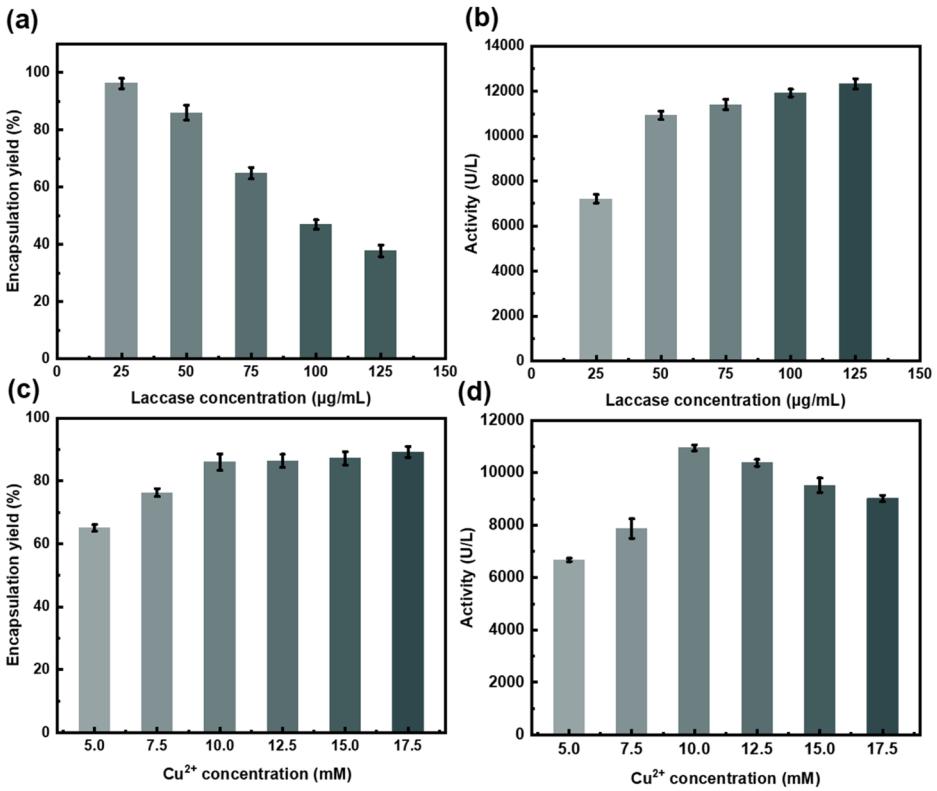

Fig. 1 Dual-phase optimization of enzyme loading and catalytic activity through laccase–Cu^{2+} coordination dynamics. Effects of laccase concentration and Cu^{2+} concentration on encapsulation yield (a and c) and enzymatic activity (b and d) in Lac-NFs. Data represent mean values ± SD of triplicates.

farnesol-induced culture conditions significantly enhanced laccase activity in *T. versicolor* through upregulation of laccase-coding genes, and morphological modification of mycelial structures.[26] Thereafter, we further confirmed that 4 mM farnesol supplementation boosted extracellular laccase activity in *T. versicolor* cultures to 6490 U L^{-1}, establishing this concentration as the baseline for subsequent nanoflower synthesis.

The formation of nanoflowers depends on the complex formed between Cu^{2+} and laccase proteins, which provides nucleation sites for copper phosphate primary crystals.[21] The number of nucleation sites increases with higher protein concentration, promoting the formation of nanoflowers and enhancing the activity of Lac-NFs. Based on this, we first investigated the effect of laccase concentration on the synthesis of Lac-NFs. While increasing laccase concentrations (25–125 μg mL^{-1}) progressively reduced encapsulation yields (EY, from 96.20% to 37.73%), it paradoxically enhanced immobilized enzyme activity (Fig. 1a and b). Notably, when the laccase concentration exceeded 50 μg mL^{-1}, the system exhibited diminishing returns in activity enhancement. This indicated a reduction in protein loading on the nanoflowers thus caused in protein waste. Therefore, the optimal laccase concentration was determined to be 50 μg mL^{-1}.

We then investigated the influence of Cu^{2+} concentration on the synthesis of Lac-NFs. Cu^{2+} titration experiments (5.0–17.5 mM) under optimal laccase loading (50 μg mL^{-1}) revealed Cu^{2+}-concentration-dependent phase transitions (Fig. 1c). The EY increased monotonically (from 66.05% to 89.28%), whereas specific activity exhibited a distinct maximum at 10 mM Cu^{2+} (Fig. 1d). This aligns with previous studies showing Cu^{2+} in $Cu_3(PO_4)_2 \cdot 3H_2O$ promoted electron transfer between the active centers of adjacent laccase molecules, thereby enhancing the enzymatic activity of the laccase–mineral hybrid complexes. However, the activity of Lac-NFs reached its maximum when the Cu^{2+} concentration reached 10 mM. Supraoptimal Cu^{2+} competed with the Cu^{2+} sites in laccase, which was closely associated with the inhibition of laccase activity, ultimately leading to a reduction in the catalytic activity of Lac-NFs.[27] Taken together, through synergistic optimization of laccase concentration (50 μg mL^{-1}) and Cu^{2+} concentration (10 mM), we achieved Lac-NFs with efficient encapsulation yield, while avoiding protein overload-induced defects and Cu^{2+} competitive inhibition.

3.1.2 Structural characterization of Lac-NFs. The morphology of Lac-NFs was characterized using SEM (Fig. 2). The prepared samples exhibited regular flower-like structures assembled from numerous interlaced nanopetals with thicknesses of approximately 18–23 nm. The average diameter of these hybrid nanoflowers, which exhibit good monodispersity, was determined to be 8–12 μm. During the nanoflower assembly process, laccase components not only induce the nucleation of copper phosphate crystals to form the scaffolds of the petals but also act as a "glue" to bond the petals together, resulting in nanoflowers with a high specific surface area.

3.1.3 Compositional characterization of Lac-NFs. The surface elemental composition of Lac-NFs was systematically characterized by X-ray photoelectron spectroscopy (XPS). As shown in Fig. 3a, the survey spectrum confirmed the coexistence of Cu, O, N, P, Cl, Na, and C, where Na and Cl originated from the phosphate buffer system, while other elements derived from laccase and $Cu_3(PO_4)_2 \cdot 3H_2O$ components, verifying the successful assembly of laccase-nanoflowers. Deconvolution of

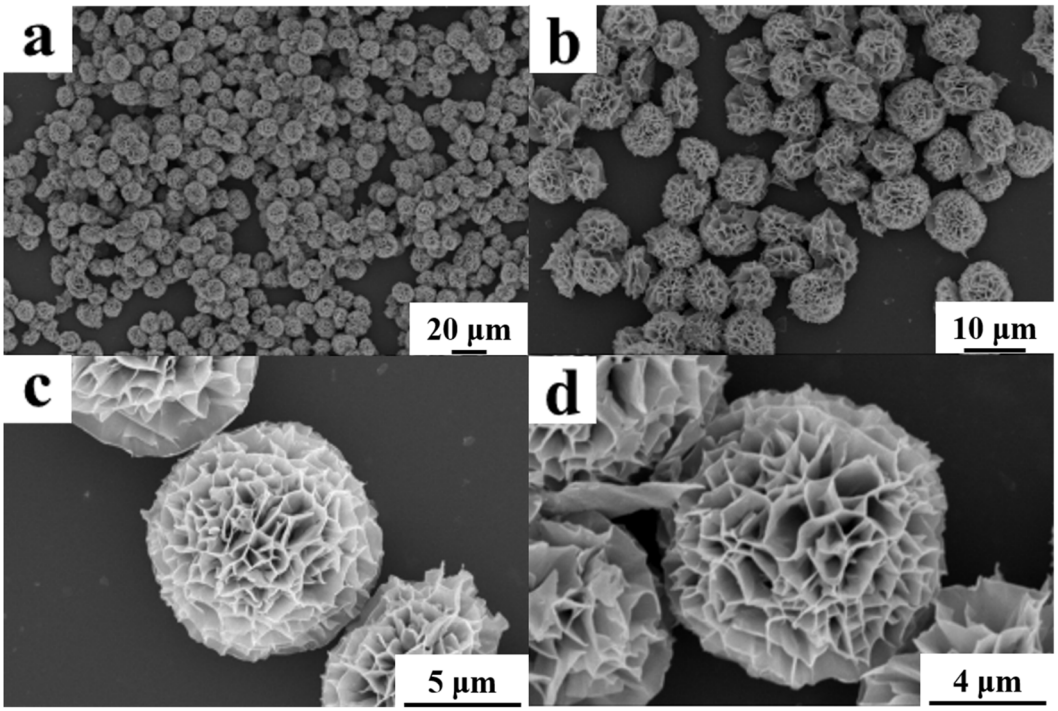

Fig. 2 Multi-scale SEM visualization of nanoflower architectural features.

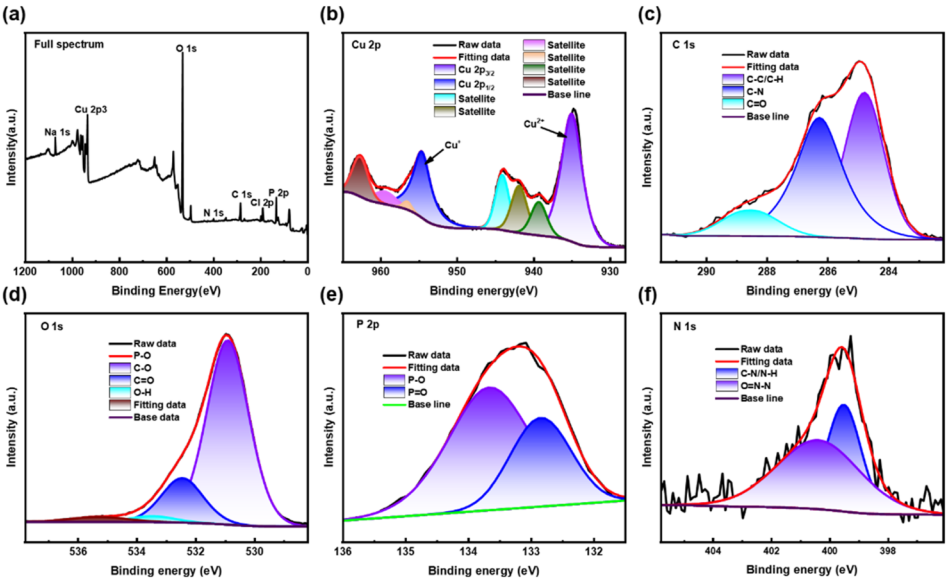

Fig. 3 XPS spectral deconvolution of Lac-NFs: (a) survey scan confirming elemental composition, with high-resolution spectra of (b) Cu^{2+} $2p_{3/2}$–$2p_{1/2}$ orbitals, (c) C 1s revealing C–C/C–O bonds, (d) O 1s showing metal–oxygen coordination, (e) P 2p phosphate signatures, and (f) N 1s amide linkages characteristic of enzyme integration.

the high-resolution spectra revealed critical chemical states: (i) Cu 2p spectrum (Fig. 3b) displayed characteristic Cu^{2+} signatures at 935.28 eV ($2p_{3/2}$) and 955.48 eV ($2p_{1/2}$) with shake-up satellite peaks;[28] (ii) C 1s spectrum (Fig. 3c) resolved three components at 284.8 eV (C–C/C–H), 286.3 eV (C–N), and 288.7 eV (C=O);[29] (iii) O 1s spectrum (Fig. 3d) exhibited four distinct contributions from P–O (530.7 eV), C–O (532.4 eV), C=O (533.5 eV), and O–H (535.3 eV);[30] (iv) P 2p spectrum (Fig. 3e) showed phosphate coordination states at 132.9 eV (P=O) and 133.7 eV (P–O);[31] (v) N 1s spectrum (Fig. 3f) revealed protein-specific bonding states at 399.6 eV (C–N/N–H) and 400.3 eV (O=N–N).[32] These spectral fingerprints collectively confirmed the successful integration of laccase within the copper phosphate matrix.

Complementing the elemental analysis, XRD characterization (Fig. 4a) demonstrated crystallographic integrity of Lac-NFs. Both Lac-NFs and pure $Cu_3(PO_4)_2 \cdot 3H_2O$ exhibited diffraction patterns matching the standard PDF# 22-0548, with characteristic peaks at $2\theta = 8.9°$, 20.5°, 26.5°, and 29.5° corresponding to (100), (111), (211), and (310) crystal planes.[33] Notably, the preserved peak positions and intensities in Lac-NFs indicated that enzyme incorporation did not disrupt the host crystal lattice, suggesting physical entrapment rather than chemical modification during immobilization.

To elucidate the molecular interactions governing enzyme immobilization, FT-IR analysis (Fig. 4b) was carried out. The FT-IR spectrum exhibited characteristic phosphate group vibrations: strong antisymmetric stretching (1100–1050 cm^{-1}) and symmetric stretching (990–960 cm^{-1}) of PO_4^{3-}, accompanied by weak antisymmetric bending (630–540 cm^{-1}) modes.[23] Protein-specific absorptions including C–H stretching vibrations (3000–2850 cm^{-1}), amide I (1680–1655 cm^{-1}), amide II (1550–

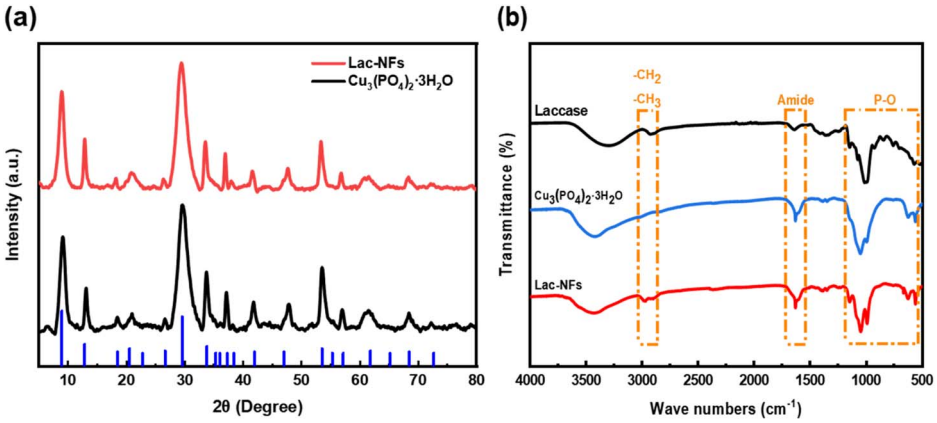

Fig. 4 XRD patterns and FT-IR spectra of Lac-NFs. (a) XRD patterns of La-NFs *versus* $Cu_3(PO_4)_2 \cdot 3H_2O$ demonstrating hybrid structure formation. (b) FT-IR spectra of La-NFs, $Cu_3(PO_4)_2 \cdot 3H_2O$, and free laccase confirming successful enzyme immobilization through interfacial interactions.

1530 cm^{-1}), amide III (1300–1260 cm^{-1}), and C–N stretching vibrations (1350–1250 cm^{-1}) were also observed. The distinct C–O stretching vibration at 1044 cm^{-1} confirmed laccase incorporation.[34] Crucially, the absence of new absorption bands or peak shifts demonstrated structural preservation of both $Cu_3(PO_4)_2 \cdot 3H_2O$ crystals and laccase, confirming physical immobilization *via* self-assembly rather than covalent bond formation.

3.2 Performance analysis of free laccase and Lac-NFs

3.2.1 Enhanced environmental adaptability of Lac-NFs over free laccase. Building upon the structural characterization, we evaluated the enzymatic properties of Lac-NFs in comparison with free laccase. As illustrated in Fig. 5a, both Lac-NFs and free laccase exhibited maximum activity at 30 °C, consistent with previous reports on immobilized *T. versicolor* laccase systems.[35] Notably, Lac-NFs demonstrated superior thermal adaptability, maintaining >80% relative activity across 20–60 °C, with a 23% activity enhancement over free enzyme at optimal temperature.

The pH-dependent profiling (Fig. 5b) revealed a significant alkaline shift in optimal pH from 4.0 (free laccase) to 6.0 (immobilized laccase), accompanied by 1.68-fold higher catalytic efficiency. Remarkably, Lac-NFs retained 47% activity at pH 8.0, outperforming free laccase by 3.7-fold-a substantial improvement over typical fungal laccases that rapidly deactivate above pH 6.[36] This pH tolerance expansion may stem from the nanoflower's charge-modulation effect: the negatively charged $Cu_3(PO_4)_2 \cdot 3H_2O$ matrix selectively repels H^+ ions, creating a localized microenvironment with reduced proton concentration that stabilizes the enzyme's tertiary structure.[37] Collectively, the immobilized system achieved dual optimization-broadening operational windows while enhancing catalytic potency. This synergistic improvement underscores the advantage of nanoflower immobilization in tailoring enzymatic performance for industrial biocatalysis.

3.2.2 Improved storage stability of Lac-NFs. We further investigated the storage stability of the Lac-NFs. Enzymatic proteins inherently suffer from activity decay during preservation due to conformational relaxation and denaturation. Comparative stability tests under controlled storage conditions (4 °C/25 °C for 30 days) revealed striking advantages of Lac-NFs. Lac-NFs demonstrated significantly enhanced stability, retaining 94.6% initial activity under refrigeration *versus* 81.43% for free laccase, while maintaining 88.43% activity at ambient conditions compared to the free enzyme's 61.63% retention (Fig. 5c and d). This represents a 1.6-fold stability enhancement under refrigeration and 1.4-fold improvement at ambient conditions, effectively addressing the storage sensitivity bottleneck of fungal laccases and positioning Lac-NFs as practical

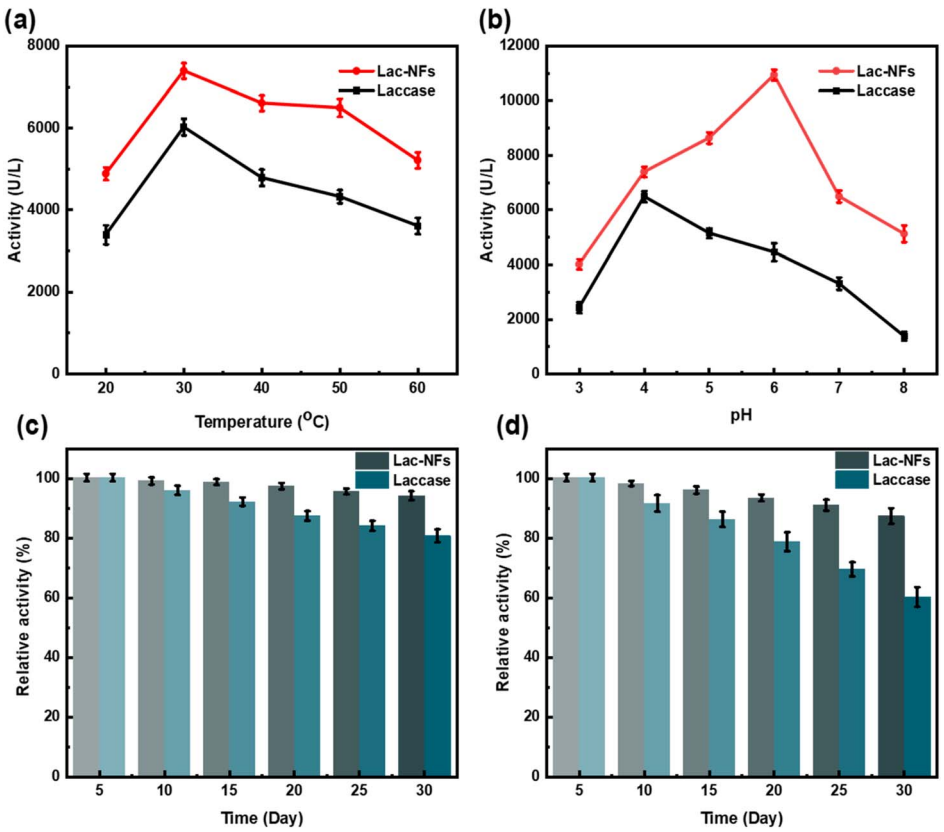

Fig. 5 Comparative biocatalytic performance of Lac-NFs *versus* free laccase: (a) temperature-dependent enzymatic activity profiles, (b) pH-responsive behavior, (c) long-term storage stability under refrigeration (4 °C), and (d) ambient storage durability (25 °C). Data represent mean values ± SD of triplicates.

biocatalysts for real-world applications. Mechanistically, the stability enhancement may originate from dual immobilization effects. Multipoint coordination between laccase's surface residues (*e.g.*, histidine, aspartate) and Cu^{2+} ions restricts molecular mobility, suppressing denaturation pathways. Additionally, phosphate-induced structural rigidification through hydrogen-bonding networks with PO_4^{3-} groups enhances conformational stability.[38] This synergistic stabilization strategy effectively decouples enzymatic activity from environmental perturbations.

3.2.3 Enzymatic kinetics and substrate affinity of Lac-NFs. To elucidate the immobilized system's catalytic advantages, followed kinetic analyses were conducted. Kinetic analysis *via* Lineweaver–Burk plots (Fig. 6a and b) revealed fundamental improvements in catalytic behavior upon immobilization: Lac-NFs demonstrated a 52.6% reduction in K_m value (Table 1, 0.83 mM for Lac-NFs *vs.* 1.75 mM for free laccase), reflecting enhanced substrate affinity through optimized ABTS diffusion within the nanoflower's hierarchical pores.[39] Concurrently, the immobilized system achieved 36.6% higher V_{max} (Table 1, 3.96 *vs.* 2.90 mM min^{-1}), indicative of improved electron transfer efficiency between adjacent laccase molecules mediated by Cu^{2+} coordination. These synergistic kinetic enhancements-reduced mass transfer limitations coupled with accelerated catalytic turnover-align coherently with the observed activity elevation, confirming the structural advantages of the nanoflower architecture in optimizing enzymatic performance.

Table 1 Enzymatic kinetics of the free laccase and the Lac-NFs

	K_m (mM)	V_{max} (mM min^{-1})	U (U L^{-1})
Free laccase	1.75 ± 0.13	2.9 ± 0.04	6490 ± 48
Lac-NFs	0.83 ± 0.06	3.96 ± 0.06	10 380 ± 125

3.3 Complete catalytic oxidation of HMF to FDCA *via* Lac-NFs

3.3.1 pH-responsive autonomous cascade catalysis for efficient HMF-to-FDCA conversion by Lac-NFs. Following the successful synthesis and comprehensive characterization of Lac-NFs, we ultimately validated their catalytic ability in the valorization of HMF using TEMPO as the redox mediators. The Lac-NFs/TEMPO system demonstrated pH-dependent catalytic dynamics in HMF oxidation, with comprehensive analysis across pH 4.0–8.0. Under acidic conditions (pH 4.0, Fig. 7a), suboptimal pH resulted in sluggish kinetics, yielding 53.72% FFCA and 46.28% FDCA after 36 h. At neutral pH 6.0 (Fig. 7b), initial rapid conversion achieved 66.55% FDCA by 36 h, though intermediate accumulation caused progressive rate deceleration. Most remarkably, alkaline conditions (pH 8.0, Fig. 7c) triggered self-optimizing catalysis: initial slow kinetics (pH > optimum) transitioned to accelerated reaction dynamics as in situ-generated carboxyl groups acidified the system, enabling complete HMF conversion within 16 h and culminating in 93.09% FDCA yield at 36 h, a 2.1-fold enhancement over neutral conditions (pH 6.0, 66.55% FDCA) and 3.7-fold improvement *versus* acidic operation (pH 4.0, 46.28% FDCA). Intermittent pH monitoring revealed the critical role of this auto-regulatory mechanism, where progressive acidification (Fig. 7d–f) dynamically maintained optimal enzymatic conformation, synergizing with TEMPO-mediated electron relay to overcome traditional pH-activity trade-offs in biocatalysis.[40] This auto-regulatory behavior, leveraging reaction-induced microenvironment modulation, positions Lac-NFs as smart biocatalysts capable of self-adapting to maximize FDCA production.

To elucidate the structural specificity underlying the superior performance of Lac-NFs, we conducted systematic control experiments comparing five catalytic systems: $Cu_3(PO_4)_2 \cdot 3H_2O$ nanosheets (NSs), free laccase (Lac), physical Lac/NSs mixtures, (bovine serum albumin) BSA-NFs, and Lac-NFs (Fig. S-5). As expected, NSs and BSA-NFs exhibited null catalytic activity and HMF remained entirely unconverted, discounting nonspecific metal/organic matrix contributions. While free laccase and Lac/NSs mixtures achieved FDCA production (≈34–38% yield), their performance remained indistinguishable, negating any synergistic enhancement from physical NSs coexistence. In stark

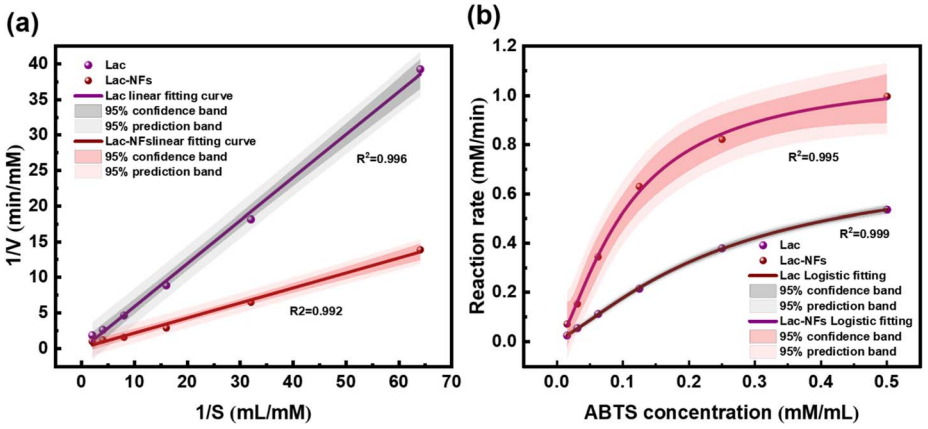

Fig. 6 Kinetic characterization of Lac-NFs: (a) Lineweaver–Burk linearization revealing improved catalytic efficiency of Lac-NFs, (b) Michaelis–Menten analysis demonstrating enhanced substrate affinity of Lac-NFs.

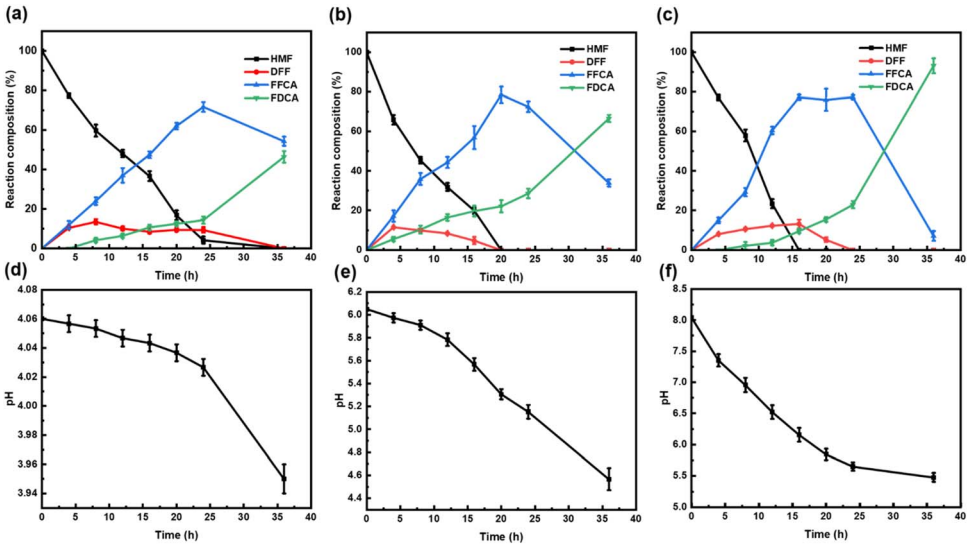

Fig. 7 pH optimization of FDCA production: (a–c) Catalytic performance under controlled initial pH conditions: (a) pH 4.0, (b) pH 6.0, (c) pH 8.0. (d–f) Real-time pH evolution corresponding to (d) condition (a), (e) condition (b), and (f) condition (c), revealing dynamic acid–base equilibrium shifts during catalytic progression. Data represent mean values ± SD of triplicates.

contrast, Lac-NFs delivered 93.09% FDCA yield under identical conditions, demonstrating that the hierarchical architecture of Lac-NFs, not merely laccase presence or copper phosphate proximity, is prerequisite for catalytic acceleration. This three-fold yield enhancement over free enzyme systems may originate from geometric confinement aligning laccase active sites for concerted TEMPO redox cycling and charge-complementary substrate channeling through phosphate-rich nanochannels.[36] The results conclusively establish that nanoflower immobilization transcends conventional carrier–enzyme interactions, creating emergent catalytic microdomains unattainable through physical mixing.

3.3.2 Rational process optimization drives full conversion of HMF-to-FDCA by Lac-NFs. Both temperature and mediator concentration significantly influenced the catalytic process of HMF by free laccase and Lac-NFs. Temperature profiling (20–60 °C at optimal pH) demonstrated the thermal robustness of Lac-NFs, achieving peak FDCA yield (94.03%) at 30 °C with 2.5× faster kinetics than free laccase (Fig. 8a). While a moderate thermal energy input enhanced molecular collisions and enzyme–substrate binding, excessive heat induced partial denaturation of free laccase and disrupt the three-dimensional structure of Lac-NFs, leading to a reduction in enzyme activity.[41]

Complementing temperature optimization, TEMPO concentration studies unveiled an electron-transfer threshold effect. The cascade mechanism initiates with laccase-mediated TEMPO oxidation to nitroxyl radicals ($TEMPO^+$), which abstract hydrogen from the hydroxymethyl group of HMF. Radical regeneration *via* enzymatic reoxidation creates sustainable redox cycling. As the TEMPO concentration increases, the catalytic sites of laccase can bind to more TEMPO molecules, which are then oxidized to nitroxyl radical cations. This process enhances the electron transfer rate, thereby increasing the FDCA yield.[41] When the TEMPO concentration reaches a specific threshold, a quantitative amount of laccase oxidizes a corresponding amount of TEMPO, at which point the electron transfer rate reaches its maximum. Concentration-dependent studies revealed a saturation threshold at 30 mM TEMPO, where Lac-NFs achieved maximum electron flux-2.4× higher FDCA yield than free laccase (Fig. 8b). This enhancement may arise from the structural advantages of the nanoflower. The hierarchical porosity synergistically concentrates $TEMPO^+$ density at catalytic interfaces, while Cu^{2+}-coordinated electron highways between adjacent laccase molecules synchronize radical regeneration cycles, collectively overcoming mass transfer constraints inherent to free enzyme systems.[42] Ultimately, the phosphate matrix plays a critical role in stabilizing radical intermediates by effectively suppressing $TEMPO^+$ dimerization, a predominant deactivation mechanism in homogeneous catalytic systems, thereby enabling sustained catalytic cycles through spatial and electronic confinement of reactive species.[43]

Systematic optimization of rationally engineered parameters (initial pH 8.0, 30 °C, 25 mM TEMPO) enabled full substrate valorization after 42 h (Fig. 8c). Real-time kinetic profiling revealed complete depletion of HMF and intermediate byproducts through synchronized oxidation cascades, while *operando* pH monitoring (Fig. 8d) uncovered progressive acidification ($\Delta pH = 2.64$), leading to a relatively slower rate of FDCA production between 36–42 h. Under strongly acidic conditions, Lac-NFs were prone to dissociation, exposing laccase protein molecules; although dissociation occurred more slowly under weakly acidic conditions, it still resulted in reduced catalytic efficiency.[44] Compared with previous studies, the reaction time for the conversion of HMF to FDCA was significantly shortened from 96 h to 42 h.[19] Moreover, the complete oxidation of HMF bypasses energy-intensive purification processes typically required in conventional systems, a critical advancement aligned with green chemistry principles.

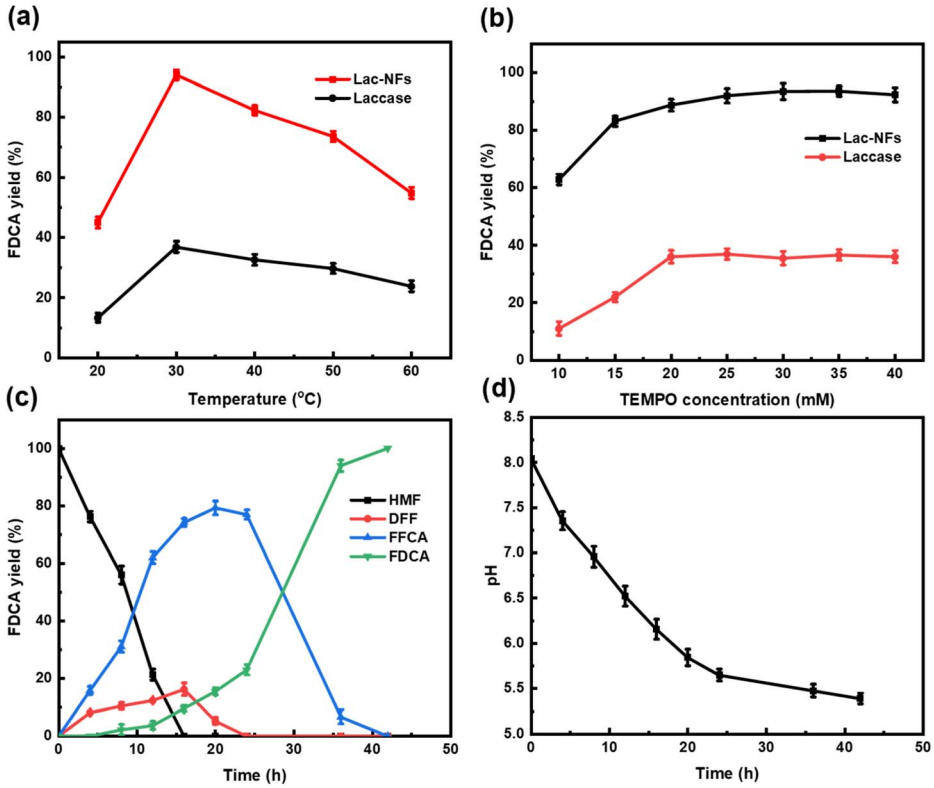

Fig. 8 Complete oxidation of HMF to FDCA by Lac-NFs under optimized conditions. (a) Thermal activation energy landscape across 20–70 °C. (b) TEMPO dosage optimization for yield enhancement. (c) Temporal evolution of HMF oxidation products demonstrating complete substrate depletion and FDCA accumulation over 42 h. (d) Corresponding pH profile revealing progressive acidification of the reaction microenvironment. Data represent mean values ± SD of triplicates.

4. Conclusions

In this study, free laccase was successfully immobilized using self-assembly technology to prepare Lac-NFs, achieving effective enzyme immobilization efficiency and significantly enhanced operational stability. The immobilized system exhibited remarkable resilience under prolonged storage and broad thermal conditions, outperforming free laccase in environmental adaptability. Crucially, the Lac-NFs/TEMPO catalytic platform enabled highly efficient and selective oxidation of HMF to FDCA. By optimizing the reaction conditions, the engineered biocatalyst enables complete substrate conversion after 42 h while eliminating downstream purification burdens. These findings establish enzyme nanoflower engineering as a transformative approach for biomass valorization, offering an eco-friendly route to FDCA production that bridges the gap between biocatalytic precision and industrial process demands.

Conflicts of interest

The authors declare that there have no conflicts of interest.

Data availability

The data supporting the findings of this study are available from the corresponding author upon reasonable request.

Table S1, Fig. S1–S5 are available in the supplementary information. See DOI: https://doi.org/10.1039/d5ra04187b.

Acknowledgements

This work is supported by the Natural Science Foundation of Shandong Province (ZR2023QC122) and the Key Research and Development Project of Shandong Province (2019GSF109079).

References

1 V. Ashokkumar, V. P. Chandramughi, G. Kumar, C. Ngamcharussrivichai, G. Piechota, B. Igliński, R. Kothari and W.-H. Chen, *Fuel*, 2024, **365**, 130751.
2 V. Bianco, L. Proskuryakova and A. Starodubtseva, *Renewable Sustainable Energy Rev.*, 2021, **146**, 111155.
3 C. Moreau, M. N. Belgacem and A. Gandini, *Top. Catal.*, 2004, **27**, 11–30.
4 N. N. Pham, C.-Y. Chen, H. Li, M. T. T. Nguyen, P. K. P. Nguyen, S.-L. Tsai, J.-Y. Chou, T. C. Ramli and Y.-C. Hu, *ACS Synth. Biol.*, 2020, **9**, 1138–1149.
5 M. G. Davidson, S. Elgie, S. Parsons and T. J. Young, *Green Chem.*, 2021, **23**, 3154–3171.
6 A. He, L. Dong, N. Xu, S. I. El-Hout, J. Xia, Z. Qiu, J. He, Y. Deng, X. Liu, L. Hu and J. Xu, *Chem. Eng. J.*, 2022, **449**, 137797.

7 D. Troiano, V. Orsat and M.-J. Dumont, *Bioresour. Technol.*, 2022, **344**, 126169.
8 M. Annatelli, J. E. Sánchez-Velandia, G. Mazzi, S. V. Pandeirada, D. Giannakoudakis, S. Rautiainen, A. Esposito, S. Thiyagarajan, A. Richel, K. S. Triantafyllidis, T. Robert, N. Guigo, A. F. Sousa, E. García-Verdugo and F. Aricò, *Green Chem.*, 2024, **26**, 8894–8941.
9 Z.-G. Zhang, Y. Yi, J.-C. Lin, D. Chen and X.-J. Ji, *Sustainable Chem. Pharm.*, 2024, **39**, 101616.
10 S. Klinyod, N. Yodsin, M. T. Nguyen, Z. Pasom, S. Assavapanumat, M. Ketkaew, P. Kidkhunthod, T. Yonezawa, S. Namuangruk and C. Wattanakit, *Small*, 2024, **20**, 2400779–2400791.
11 L. Li, Y. Wang, Y. Ruan, T. Xu, S. Wu and W. Lu, *Appl. Surf. Sci.*, 2024, **672**, 160771–160783.
12 H. Liu, J. Zhang, X. Li, R. Zhang, W. Jia, J. Zhang, Y. Sun and L. Peng, *Appl. Catal., B*, 2025, **365**, 124994–125005.
13 A. Swoboda, S. Zwölfer, Z. Duhović, M. Bürgler, K. Ebner, A. Glieder and W. Kroutil, *ChemSusChem*, 2024, **17**, e202400156.
14 K. A. P. Payne, S. A. Marshall, K. Fisher, M. J. Cliff, D. M. Cannas, C. Yan, D. J. Heyes, D. A. Parker, I. Larrosa and D. Leys, *ACS Catal.*, 2019, **9**, 2854–2865.
15 P. Bhardwaj, N. Kaur, M. Selvaraj, H. A. Ghramh, B. M. Al-Shehri, G. Singh, S. K. Arya, K. Bhatt, S. Ghotekar, R. Mani, S. W. Chang, B. Ravindran and M. K. Awasthi, *Bioresour. Technol.*, 2022, **364**, 128031–12803146.
16 M. A. do Nascimento, B. Haber, M. R. B. P. Gomez, R. A. C. Leão, M. Pietrowski, M. Zieliński, R. O. M. A. de Souza, R. Wojcieszak and I. Itabaiana, *Green Chem.*, 2024, **26**, 8211–8219.
17 K. Saikia, A. K. Rathankumar, P. S. Kumar, G. Rangasamy, V. K. Vaithyanathan and V. K. Vaidyanathan, *Chemosphere*, 2022, **308**, 136567.
18 K. Lin, A. Xia, Y. Huang, X. Zhu, X. Zhu, K. Cai, Z. Wei and Q. Liao, *Bioresour. Technol.*, 2023, **374**, 128775.
19 K. F. Wang, C. l. Liu, K. y. Sui, C. Guo and C. Z. Liu, *ChemBioChem*, 2018, **19**, 654–659.
20 X. Chang, C. Zhang, L. Gao, X. Liu, S. You, W. Qi, K. Wang, X. Guo, R. Su, H. Lu and Z. He, *Trans. Tianjin Univ.*, 2019, **25**, 488–496.
21 J. Ge, J. Lei and R. N. Zare, *Nat. Nanotechnol.*, 2012, **7**, 428–432.
22 M. Bilal, M. Asgher, S. Z. H. Shah and H. M. N. Iqbal, *Int. J. Biol. Macromol.*, 2019, **135**, 677–690.
23 G. He, W. Hu and C. M. Li, *Colloids Surf., B*, 2015, **135**, 613–618.
24 M. R. Zhang, Y. Zhang, C. K. Yang, C. Y. Ma, Y. H. Zhang and J. G. Tang, *Int. J. Biol. Macromol.*, 2021, **188**, 783–789.
25 S. S. Maurya, S. S. Nadar and V. K. Rathod, *J. Biotechnol.*, 2020, **317**, 27–33.
26 K.-F. Wang, C. Guo, F. Ju, N. A. Samak, G.-Q. Zhuang and C.-Z. Liu, *Sci. Rep.*, 2018, **8**, 15213–15221.
27 K. Sun, S. Li, J. Yu, R. Gong, Y. Si, X. Liu and G. Chu, *Chemosphere*, 2019, **225**, 745–754.
28 T. D. Tran, P. T. Nguyen, T. N. Le and M. I. Kim, *Biosens. Bioelectron.*, 2021, **182**, 113187–113195.
29 J. Han, P. Luo, L. Wang, J. Wu, C. Li and Y. Wang, *ACS Appl. Mater. Interfaces*, 2020, **12**, 15023–15033.
30 J. Guo, Y. Wang and M. Zhao, *Sens. Actuators, B*, 2019, **284**, 45–54.
31 J. G. Acheson, L. Robinson, S. McKillop, S. Wilson, M. J. McIvor, B. J. Meenan and A. R. Boyd, *Mater. Charact.*, 2021, **171**, 110739–110750.
32 V. P. Hitaishi, R. Clément, L. Quattrocchi, P. Parent, D. Duché, L. Zuily, M. Ilbert, E. Lojou and I. Mazurenko, *J. Am. Chem. Soc.*, 2019, **142**, 1394–1405.
33 C. Gulmez, C. Altinkaynak, N. Özdemir and O. Atakisi, *Int. J. Biol. Macromol.*, 2018, **119**, 803–810.
34 I. Lee, H. J. Cheon, M. D. Adhikari, T. D. Tran, K.-M. Yeon, M. I. Kim and J. Kim, *Int. J. Biol. Macromol.*, 2020, **155**, 1520–1531.
35 K. Jankowska, J. Zdarta, A. Grzywaczyk, E. Kijeńska-Gawrońska, A. Biadasz and T. Jesionowski, *Environ. Res.*, 2020, **184**, 109332–109342.
36 F. Lassouane, H. Aït-Amar, S. Amrani and S. Rodriguez-Couto, *Bioresour. Technol.*, 2019, **271**, 360–367.
37 S. Noreen, S. Perveen, N. Shafiq, S. Aslam, H. M. N. Iqbal, S. S. Ashraf and M. Bilal, *Environ. Technol. Innovation*, 2021, **24**, 101884–101894.
38 Z. Han, H. Wang, J. Zheng, S. Wang, S. Yu and L. Lu, *Environ. Res.*, 2023, **216**, 114690–114701.
39 J. George, A. K. Alanazi, P. Senthil Kumar, S. Venkataraman, D. S. Rajendran, J. K. Athilakshmi, I. Singh, I. Singh, P. sen, M. Purushothaman, P. A. Balakumaran, V. K. Vaidyanathan and H. M. Abo-Dief, *Chemosphere*, 2023, **331**, 138734–138743.
40 J. Wu, X. Ma, C. Li, X. Zhou, J. Han, L. Wang, H. Dong and Y. Wang, *Chem. Eng. J.*, 2022, **427**, 131808–131818.
41 L. Wang, T. Yuan and Y. Zhang, *Food Chem.*, 2024, **24**, 101916–101926.
42 H. Chen, L. An, M. Li, H. Liu, Z. Jin, H. Ma, J. Ma, J. Zhou, R. Duan, D. Zhang, X. Cao, T. Wang and X. Wu, *Food Chem.*, 2024, **445**, 138756.
43 A. C. Cardiel, B. J. Taitt and K.-S. Choi, *ACS Sustain. Chem. Eng.*, 2019, **7**, 11138–11149.
44 K. A. Al-Maqdi, N. Elmerhi, A. Alzamly, I. Shah and S. S. Ashraf, *J. Water Process Eng.*, 2023, **51**, 103438.